Broadband and lossless lithium niobate valley photonic crystal waveguide [Invited]

Rui Ge (葛 睿), Xiongshuo Yan (颜雄硕), Yuping Chen (陈玉萍)[*], and Xianfeng Chen (陈险峰)

State Key Laboratory of Advanced Optical Communication Systems and Networks, School of Physics and Astronomy, Shanghai Jiao Tong University, Shanghai 200240, China

We investigate the influences of structure parameters and interface shapes on the bandwidth of the edge state of lithium niobate valley photonic crystals. By increasing the size difference of two air holes in the same unit cell, we find that the bandwidth of the lossless nontrivial edge state possesses a peak value of $0.0201(a/\lambda)$, which can be used to construct broadband valley photonic crystal waveguides. Mode field distributions verify that the waveguide is robust against sharp bends and exhibits chirality. When the unit cell is arranged in a bearded interface with the top and bottom components showing negative and positive valley Chern numbers, respectively, we find that the lithium niobate valley photonic crystal is more likely to exhibit a lossless edge state, which is difficult to be realized in valley waveguides with low refractive index materials. This work can provide guidance on the design of the high-performance topological waveguide.

Keywords: lithium niobate; valley photonic crystal waveguide; propagation loss.

DOI: 10.3788/COL202119.060014

1. Introduction

The topological valley edge state has recently attracted extensive attention owing to its superior properties like robustness to sharp bends and shows unique Bloch modes with chirality[1–4]. Researchers have proposed many methods to fulfill valley edge states in photonic crystals, which are mainly based on the same principle where constructing two parts of unit cells that show reversed symmetry with each other allows the top and bottom structures to show opposite valley Chern numbers. Previous works about valley edge states typically focus on their topological protection effect, bandwidth, and loss property[3–5]. Obtaining a broadband valley waveguide that is simultaneously chiral, lossless, and robust is also a vital goal when designing topological optical waveguides.

It is generally simple to realize a lossless valley Hall waveguide with large bandwidth in a Si photonic crystal owing to its high refractive index of ~3.47. However, in some conditions, we need to construct valley waveguides with low refractive index materials, for instance, materials with piezoelectric effects, electro-optic effects, or pyroelectric effect are desired to flexibly control the refractive index of the background material of topological photonic crystals by adjusting the external pressure or external electric field. These materials typically possess low refractive index, e.g., $LiNbO_3$, lithium niobate (LN) for 2.1–2.2[6,7], liquid crystal for ~1.45 − 1.75, and $BaTiO_3$ for 2.2–2.3, which pushes the edge state to the high-frequency realm, and achieving a large

bandwidth lossless edge state based on these materials becomes significant. Liquid crystal and $BaTiO_3$ have been already used to design a tunable valley photonic crystal beam splitter[8], optical switch[9], and waveguide[10]. These works usually use the devices sandwiched by metal slabs to confine light in the z direction. Consequently, the loss property of valley photonic crystals that consist of low refractive index materials becomes significant.

In this paper, we investigate the influences of structure parameters and interface shapes on the bandwidth of the edge state in Z-cut LN valley photonic crystal waveguides. Then, the edge state with a bandwidth of $0.0201(a/\lambda)$ can be obtained. Moreover, the robustness and chirality of the proposed structure are also verified. Finally, bandwidths of different types of LN valley photonic crystal interfaces are analyzed. It is noted that for LN valley photonic crystal waveguides, a lossless edge state is more likely to show up when the unit cells construct the bearded interface with top and bottom components showing negative and positive valley Chern numbers, respectively.

2. Theoretical Model and Analysis

Firstly, we consider the configuration proposed in Ref. [2], as shown in Fig. 1(a). It is constituted by a unit cell of a circle hole with the larger radius r_1 and another circle hole with the smaller radius of r_2, and the unit cells of the upper-half (top part) and the lower-half (bottom part) of the photonic crystal are reversed.
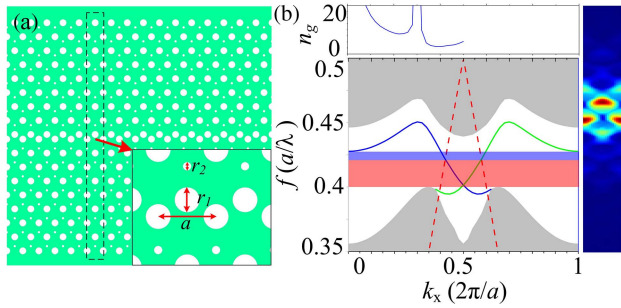
Fig. 1. (a) Schematic of the "bearded" interface composed of unit cells with negative and positive valley Chern numbers in the top and bottom components, respectively, and (b) the corresponding projected band diagram, group index diagram when $r_1 - r_2 = 0.1857a$, and $|H_z|$ field distribution at $k_x = 0.4 \, (2\pi/a)$.

The interface of two photonic crystal tiles is like a "bearded" shape[2,11].

We set the lattice constant to $a = 0.7 \, \mu m$, $r_1 = r_2 = 0.1 \, \mu m = 0.1428a$, the slab thickness to $0.35 \, \mu m = 0.5a$, and the refractive index of the slab to 2.143[12] for LN as the initial structure parameters. When the photonic crystal is in the initial parameter, the Dirac point will show up, and, if we set r_1 to no longer equal r_2, the degeneracy point will break up. It should be noted that when $r_1 = 0.2 \, \mu m$ and $r_2 = 0 \, \mu m$, the Berry curvature of the top and bottom parts will vanish, however, the structure also exhibits chirality and robustness, which is verified in previous works[13], and we also take this condition into consideration. When referring to the valley Chern number, we only consider the lowest transverse electric (TE) band at the K and K' points for convenience. All of the results in this work are excited by TE modes since the structure shows no band gap for the transverse magnetic (TM) mode. The configuration shows a negative valley Chern number in the top part and a positive valley Chern number in the bottom part[2]. The group index of the edge state is defined as $n_g = |(1/c) \cdot (\partial k/\partial \omega)|$[4,14].

To clearly demonstrate the loss behavior of photonic crystals, we plot the projected band diagram and group index diagram of the LN valley photonic crystal with the bearded interface when $r_1 - r_2 = 0.1857a = 0.13 \, \mu m$, as shown in Fig. 1(b). The simulated area is plotted in the black dash box in Fig. 1(a). The edge state bands with blue and green colors are locked with opposite chiral waves, and the blue and red areas represent the frequency region beyond and blow the light line, which is shown using a red dotted line. The bulk bands are demonstrated with gray color. It can be inferred that if we focus on a fixed chirality, the frequency edge state gradually increases until $k_x = 0.4(2\pi/a)$ and then drops. That is to say, when the nonreciprocal vector sweeps from Γ to X, the edge state moves down to a lower frequency, although it ascends initially. For convenience, we define this type of edge state as "Γ–X descending shape." The group index n_g diagram indicates that when k_x sweeps from Γ to X, n_g first drops to a low value, then rises to an ultra-large value, and finally drops fiercely. The results in the group index

diagram are identical to those in the projected band diagram in Fig. 1(b). We also observe that a large bandwidth edge state exists below the light line, which means that the edge state is both chiral and lossless. Therefore, this kind of interface is an excellent platform for the topological valley edge state in LN photonic crystals.

Meanwhile, as the radius difference between two holes $(r_1 - r_2)$ gradually increases, the frequency ranges of edge states above and below the light line, e.g., lossy and lossless chiral edge states, are obtained as shown in Figs. 2(a) and 2(b). The results show that when $r_1 - r_2$ increases, the top and bottom frequencies of both edge states become larger. They show the largest bandwidths of lossless or total edge states of $0.0386(a/\lambda)$ and $0.0315(a/\lambda)$ simultaneously at $r_1 - r_2 = 0.2857a = 0.2 \, \mu m$.

However, the simulated results indicate that the band at the higher frequency of the bearded interface LN valley photonic crystal is immune to sharp bends, which is topologically nontrivial. Nevertheless, the band at the lower frequency is sensitive to sharp bends, which is topologically trivial. Similar results have already been discovered in the bearded interface with positive and negative valley Chern numbers in the top and bottom parts of valley photonic crystals[15,16], respectively. We only care about the edge state that is simultaneously lossless, chiral, and robust. We gradually increase the difference between two holes $(r_1 - r_2)$, and the frequency ranges of lossy and lossless nontrivial edge states are obtained, as shown in Figs. 2(c) and 2(d). The results show that the bandwidth of both states shows a peak value. Meanwhile, we plotted the transmission contrast of the
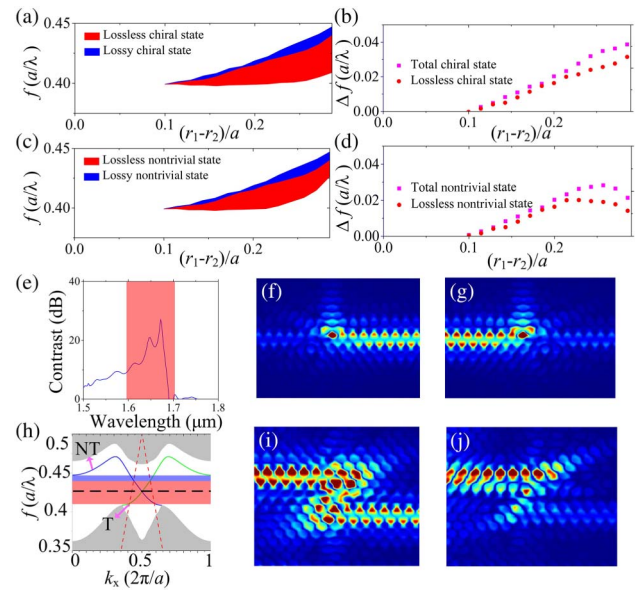

Fig. 2. Evolution of (a), (b) chiral and (c), (d) nontrivial state frequency and the corresponding bandwidth of the bearded LN valley photonic crystal as a function of $r_1 - r_2$. (e) Transmission contrast and (f), (g) the corresponding $|H_z|$ field distributions when the source is set to show two opposite chiralities. (h) Band diagram of LN valley photonic crystal when $r_1 - r_2 = 0.2857a$, and (i), (j) $|H_z|$ field distributions excited by a plane wave source at $\omega = 0.435 \, (2\pi/a)$ and $\omega = 0.42 \, (2\pi/a)$.
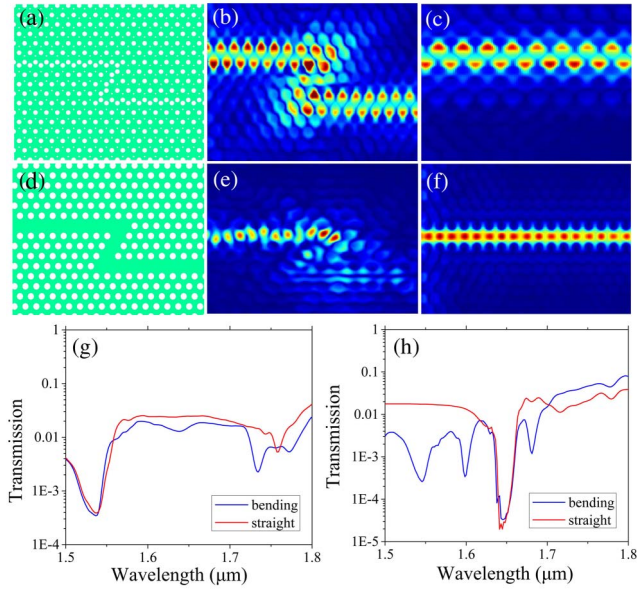
Fig. 3. (a) Structure of the proposed broadband valley LN photonic crystal waveguide with a sharp bend. The $|H_z|$ field distributions of (b) the waveguide with the sharp bend and (c) the straight waveguide at $\omega = 0.42$ $(2\pi/a)$. (d) Structure of trivial LN photonic crystal waveguides with sharp bend. The $|H_z|$ field distributions of (e) the waveguide with the sharp bend and (f) the straight waveguide at $\omega = 0.42$ $(2\pi/a)$. (g), (h) Transmission spectra for the topological and ordinary waveguides.

waveguide when the sources are two dipoles with an initial phase difference of ±90° and orthogonal polarization directions, as shown in Fig. 2(e).

The structure shows a broadband chiral bandwidth. The $|H_z|$ field distributions in Figs. 2(f) and 2(g) show that the energy can pass through the waveguide directionally. The band structure in Fig. 2(h) verified that the edge states at the higher and lower frequencies are both locked with the same chirality. $|H_z|$ field distributions in Figs. 2(i) and 2(j) show that the energy at $0.42(a/\lambda)$ cannot pass through sharp bend, while the energy at $0.435(a/\lambda)$ can pass through sharp bend, which means that these are actually two different edge states, and we separate them using a black dotted line. The bandwidth of the robust, lossless, and chiral edge state obtains a maximum value of $0.0201(a/\lambda)$ at $r_1 - r_2 = 0.2285a$, which is chosen as the optimized parameter.

The comparison of the topological waveguide and ordinary waveguide is shown in Fig. 3. The schematic of the topological waveguide is shown in Fig. 3(a). The $|H_z|$ field distributions in Figs. 3(b) and 3(c) demonstrate that the energy can pass through the sharp bend or straight bend. While for the ordinary waveguide in Fig. 3(d), the $|H_z|$ field distributions in Figs. 3(e) and 3(f) demonstrate that the energy cannot pass through the sharp bend. We also plotted the transmission spectra of the waveguide with and without bend for topological and ordinary waveguides, respectively. The results in Figs. 3(g) and 3(h) indicate that the transmission spectrum for the topological waveguide shows the negligible difference between two configurations, while the one for the ordinary waveguide shows much difference.

In Fig. 4, we analyze the loss properties of valley photonic crystals with different interfaces. We plot the band diagram and group index diagram using a bearded interface configuration similar to the design in Fig. 1. The positions of the large hole and the small hole are swapped as shown in Fig. 4(a). This structure was already researched in Refs. [17,18] and possesses positive valley Chern numbers in the top part and negative Chern numbers in the bottom part[2]. The band structure in Fig. 4(b) shows trivial and nontrivial topological edge states, which possess opposite chirality. Meanwhile, the trivial edge state that is not robust against sharp bends is located at a higher frequency, and the nontrivial edge state that is immune to sharp bends is located at a lower frequency[15]. The result implies that both edge states are lossy. The group index diagrams in Fig. 4(b) indicate that n_g of both edge states first drop to low values, then rise to ultra-large values, drop fiercely, and finally rise to ultra-large values.

Figures 4(c) and 4(d) demonstrate the structure, band diagram, and group index diagram using the zigzag interface configuration, which are already researched in Refs. [18–20] and possess positive valley Chern numbers in the top part and negative Chern numbers in the bottom part[13,17]. We plotted the projected band diagram $r_1 - r_2 = 0.1714a$, and it can be inferred that the edge state moves to higher frequencies and finally shows a shallow drop, which we define as "Γ–X ascending shape." We find that the reason why all edge states are above the light line lies in that the edge state band starts to become flat near $k_x = 0.5(\pi/a)$, which is not desired, and this phenomenon was also observed in Ref. [20]. The n_g in Fig. 4(d) shows similar behaviors as those in Fig. 4(b).
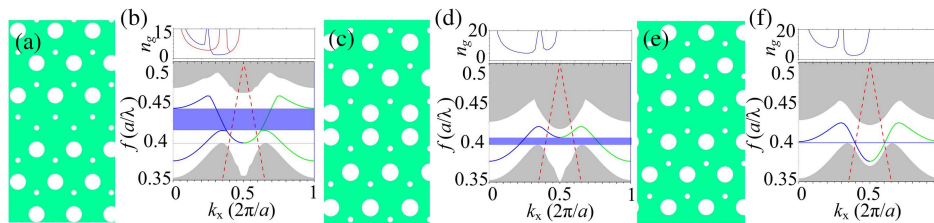

Fig. 4. Schematics of (a), (b) the bearded interface and (c)–(f) the zigzag interface composed of circle holes and their corresponding projected band diagrams and group index diagrams. In (a) and (e), the unit cells possess positive and negative valley Chern numbers in the top and bottom parts, while in (c) the unit cells possess negative and positive valley Chern numbers in the top and bottom parts.

Figures [4(e)] and [4(f)] demonstrate the structure, band diagram, and group index diagram using a zigzag interface configuration, which is the same as in Fig. [4(c)], while the small and large holes are swapped. The structure is already researched in Ref. [18] and possesses negative valley Chern numbers in the top part and positive Chern numbers in the bottom part[17]. The band of the edge state behaves in a "Γ–X descending shape." While the lossless edge state does not occur owing to the descending amplitude being small, the bandwidth of the band is small, so the eigen field distribution is difficult to obtain. The n_g in Fig. [4(f)] shows similar behaviors as those in Fig. [4(b)].

Consequently, we can infer the two vital issues to obtain the lossless edge state in hole-type LN valley photonic crystals. The one is the band of edge state with "Γ–X descending shape," and the other is that the amplitude of the descending frequency must be large. "Γ–X descending shape" can be realized by arranging arrays of air hole unit cells with negative valley Chern numbers in the top part and with positive valley Chern numbers in the bottom part. Obviously, the zigzag interface and bearded interface both can produce the "Γ–X descending shape," while for the zigzag interface the descending amplitude is too small. Consequently, the bearded interface with negative and positive valley Chern numbers in the top and bottom parts is more desired.

3. Conclusions

In conclusion, we analyze the bandwidth and loss properties of bearded interface LN valley photonic crystal waveguides. The maximum bandwidth of the lossless, chiral, and robust edge state is $0.0201(a/\lambda)$. In order to achieve large bandwidth lossless LN valley photonic crystals, we deduce that the band of edge state behavior must show a "Γ − X" descending shape," which can be realized by using the bearded interface and ensuring that the valley Chern number of the top part is negative, while the one in the bottom part is positive. This work is supposed to provide guidance to high-performance topological devices, and the results can be extended to other materials that have low refractive index such as $LiTaO_3$ and $BaTiO_3$.

Acknowledgement

References

1. T. Ma and G. Shvets, "All-Si valley-Hall photonic topological insulator," New J. Phys. **18**, 025012 (2016).
2. X. T. He, E. T. Liang, J. J. Yuan, H. Y. Qiu, X. D. Chen, F. L. Zhao, and J. W. Dong, "A silicon-on-insulator slab for topological valley transport," Nat. Commun. **10**, 872 (2019).
3. E. Sauer, J. P. Vasco, and S. Hughes, "Theory of intrinsic propagation losses in topological edge states of planar photonic crystals," Phys. Rev. Res. **2**, 043109 (2020).
4. E. Nussbaum, E. Sauer, and S. Hughes, "Inverse design of broadband and lossless topological photonic crystal waveguide modes," Opt. Lett. **46**, 1732 (2021).
5. W. Noh, H. Nasari, H. M. Kim, Q. L. Van, Z. Jia, C. H. Huang, and B. Kante, "Experimental demonstration of single-mode topological valley-Hall lasing at telecommunication wavelength controlled by the degree of asymmetry," Opt. Lett. **45**, 4108 (2020).
6. C. Lu, B. Zhu, C. Zhu, L. Ge, Y. Liu, Y. Chen, and X. Chen, "All-optical logic gates and a half-adder based on lithium niobate photonic crystal microcavities," Chin. Opt. Lett. **17**, 072301 (2019).
7. H. Jiang, X. Yan, H. Liang, R. Luo, X. Chen, Y. Chen, and Q. Lin, "High harmonic optomechanical oscillations in the lithium niobate photonic crystal nanocavity," Appl. Phys. Lett. **117**, 081102 (2020).
8. Y. Wang, W. Zhang, and X. Zhang, "Tunable topological valley transport in two-dimensional photonic crystals," New J. Phys. **21**, 093020 (2019).
9. Y. Wu, X. Hu, and Q. Gong, "Reconfigurable topological states in valley photonic crystals," Phys. Rev. Mater. **2**, 122201 (2018).
10. F. Chen, "The tunable topological valley states in designer surface plasmon crystals based on liquid crystals," in *2020 IEEE MTT-S International Conference on Numerical Electromagnetic and Multiphysics Modeling and Optimization (NEMO)* (IEEE, 2020), p. 1.
11. B. Orazbayev and R. Fleury, "Quantitative robustness analysis of topological edge modes in C6 and valley-Hall metamaterial waveguides," Nanophotonics **8**, 1433 (2019).
12. S. Duan, Y. Chen, G. Li, C. Zhu, and X. Chen, "Broadband polarization beam splitter based on a negative refractive lithium niobate photonic crystal slab," Chin. Opt. Lett. **14**, 042301 (2016).
13. J. K. Yang, Y. Hwang, and S. S. Oh, "Evolution of topological edge modes from honeycomb photonic crystals to triangular-lattice photonic crystals," arXiv:2012.14760 (2020).
14. Y. Gong, S. Wong, A. J. Bennett, D. L. Huffaker, and S. S. Oh, "Topological insulator laser using valley-Hall photonic crystals," ACS Photon. **7**, 2089 (2020).
15. M. J. Mehrabad, A. P. Foster, R. Dost, E. Clarke, P. K. Patil, A. M. Fox, M. S. Skolnick, and L. R. Wilson, "Chiral topological photonics with an embedded quantum emitter," Optica **7**, 1690 (2020).
16. H. Yoshimi, T. Yamaguchi, Y. Ota, Y. Arakawa, and S. Iwamoto, "Slow light waveguides in topological valley photonic crystals," Opt. Lett. **45**, 2648 (2020).
17. Z. Yang, S. Aghaeimeibodi, and E. Waks, "Chiral light–matter interactions using spin-valley states in transition metal dichalcogenides," Opt. Express **27**, 21367 (2019).
18. P. Yang, P. Jiang, X. Guo, and L. Hou, "Topologically protected Mach–Zehnder interferometer," J. Opt. **22**, 105001 (2020).
19. M. Shalaev, W. Walasik, A. Tsukernik, Y. Xu, and N. M. Litchinister, "Robust topologically protected transport in photonic crystals at telecommunication wavelengths," Nat. Nanotechnol. **14**, 31 (2019).
20. Y. Zeng, U. Chattopadhyay, B. Zhu, B. Qiang, J. Li, Y. Jin, L. Li, A. G. Davies, E. H. Linfield, B. Zhang, Y. Chong, and Q. J. Wang, "Electrically pumped topological laser with valley edge modes," Nature **578**, 246 (2020).